Pavel A. Perezhogin*

2D turbulence closures for the barotropic jet instability simulation

https://doi.org/10.1515/rnam-2020-0003
Received June 3, 2019; accepted December 13, 2019

Abstract: In the present work the possibility of turbulence closure applying to improve barotropic jet instability simulation at coarse grid resolutions is considered. This problem is analogous to situations occurring in eddy-permitting ocean models when Rossby radius of deformation is partly resolved on a computational grid. We show that the instability is slowed down at coarse resolutions. As follows from the spectral analysis of linearized equations, the slowdown is caused by the small-scale normal modes damping arising due to numerical approximation errors and nonzero eddy viscosity. In order to accelerate instability growth, stochastic and deterministic kinetic energy backscatter (KEBs) parameterizations and scale-similarity model were applied. Their utilization led to increase of the growth rates of normal modes and thus improve characteristic time and spatial structure of the instability.

Keywords: Two-dimensional turbulence, stochastic parameterization, kinetic energy backscatter, subgrid scale modelling, scale-similarity, normal modes, barotropic instability.

MSC 2010: 76F06, 76F65, 76E20, 65L07, 81T80, 76M55, 76M20, 76M35

The characteristic spatial scale of geophysical flows is determined by the Rhines scale where, under the interplay of turbulence and Rossby waves, jet currents occur [34, 39]. This scale for the ocean is approximately an order less than for the atmosphere [34]. Due to this reason, numerical ocean models used in climate research usually resolve mesoscale variability just partly instead of the atmosphere models [12]. These ocean models are called 'eddy-permitting' models. Thus, the development of efficient numerical solvers taking into consideration both unresolved turbulence and numerical schemes is primarily necessary for the numerical ocean models. In [30] and [33] we evaluated numerical schemes and turbulence closures in developed 2D turbulence simulation. This work extends our studies to the case of transition to turbulence.

In this work, we consider large eddy simulations (LES) [10] of quasi-2D geophysical flows. This methodology implies that the most energetic eddies responsible for the main features of the flow are reasonably resolved on the computational grid. To make equations for the resolved scales closed, we have to construct subgrid scale (SGS) closure (or SGS parameterization) which models in some way influence of unresolved scales on resolved ones. In general, construction of closures for 2D turbulence is rather more sophisticated than for 3D turbulence since inviscid dynamics in 2D case possesses infinite set of invariants called Casimirs [11, 31, 32, 35]. One of Casimirs is enstrophy (squared vorticity). It plays the major role in ability of 2D turbulence to transfer energy to large scales. SGS closures for the quasi-2D turbulence are usually based on the KLB (Kraichnan-Leith-Batchelor) theory [5, 23, 24]. This theory predicts redistribution of the enstrophy and kinetic energy into small and large scales, respectively. Thus, we mention two major groups of parameterizations approximately satisfying these properties. Eddy viscosity models (EVM) [19, 38] describe enstrophy transfer from resolved scales to unresolved ones. Kinetic energy backscatter (KEB) parameterizations [6, 9, 14, 15, 21, 22, 36, 37, 40] inject energy into the resolved scales. The property of the energy redistribution into large scales is equivalent to conservation of energy by resolved flow. It can be satisfied by combining EVM and KEB parameterizations in such a way to energy of resolved flow to be conserved ('energetically consistent' KEB [21, 22, 40]). SS (scale-similarity, [4]) model can be viewed as alternative SGS model which utilizes similarity between scales to construct nonlinear model mimicking redistribution of energy and enstrophy be-

***Corresponding author: Pavel A. Perezhogin,** Marchuk Institute of Numerical Mathematics of the Russian Academy of Sciences, Moscow 119333, Russia. E-mail: pperezhogin@gmail.com

tween resolved and unresolved scales [33]. It is extensively used in 3D turbulence simulations [18], but in 2D turbulence there are only a few examples [7, 28, 33].

We have tested mentioned above SGS models in homogeneous 2D turbulence in [33] and have shown them to improve statistical features of large scales. Bearing in mind that developed turbulence and quasi-stationary laminar jet currents coexist together in the ocean, they are both influenced by the same SGS closure. Thus, it is of substantial interest for us to know how do these closures work at the laminar-turbulent transition (LTT) of jet current when barotropic instability develops. Although baroclinic instability is the primary mechanism of the jet currents destruction in the ocean [13], we investigate here barotropic instability since KEB closures are designed to capture properties of barotropic turbulence. For our knowledge, SGS closures have never been tested in 2D LTT. Also, we notice that in contrast to developed turbulence where fully non-linear dynamics occurs, barotropic instability can be treated in linear approximation, which allows us to give simple analytical considerations about SGS models properties.

Simulation of barotropic jet instability is widely used for testing of global atmospheric numerical models in shallow water approximation [16]. In this benchmark, barotropic instability is initiated by the Gaussian perturbation in the height field, and the resulting solutions are used to evaluate convergence properties of numerical schemes. We notice that this setting is not suitable for the SGS closures testing since these closures capture only statistical properties of unresolved scales and there is no guaranty for them to improve prediction skill of the coarse model. For this reason, we have developed a framework for the statistical analysis of barotropic instability simulation.

In this work, we study barotropic instability simulation at coarse resolutions of the computational grid. We consider one-layer barotropic equations in a doubly-periodic channel, using unstable jet current as the initial condition. Instability is initiated by the white noise in time stochastic forcing simulating the effect of the atmosphere on the ocean. Using statistical averaging over an ensemble of realizations of stochastic forcing, we decompose the flow into the mean flow and the turbulent fluctuations. Turbulence Kinetic Energy (TKE) and its distribution over normal modes were chosen to be the primary statistical properties of the barotropic instability. For the models with coarse mesh resolution, we show the reduction of the growth rates of normal modes compared to reference simulation at high resolution. There are two reasons for this: strong eddy viscosity and numerical schemes used. Eddy viscosity turns out to be the main reason for the slowdown of instability growth since it smooths out the jet current. We propose to use negative viscosity and stochastic KEB parameterizations [21] and scale-similarity model (SS) [4] to restore statistical properties of barotropic instability. Application of these parameterizations leads to acceleration of instability growth in three different ways. So, negative viscosity KEB [21] increases the growth rates of normal modes by modifying mean flow, stochastic KEB [21] increases their pre-exponentials and SS model increases growth rates by modifying linearized system. Different mechanisms of negative viscosity KEB and SS models allows us to combine them together which gives growth rates in coarse model the most close to ones found in reference simulation.

1 Governing equations

Consider a 2D incompressible fluid on a channel $\Omega = (0, 2\pi)^2$ with Cartesian coordinates $(x, y) \equiv (x_1, x_2) \in \Omega$ and doubly-periodic boundary conditions. The velocity field, $\mathbf{u} = (u_x, u_y)^T \equiv (u_1, u_2)^T$, T – transpose, evolves according to the equations:

$$\frac{\partial \mathbf{u}}{\partial t} + (\mathbf{u} \cdot \nabla)\mathbf{u} = -\nabla p + \mathbf{D} + \mathbf{F} \tag{1.1}$$

$$\nabla \cdot \mathbf{u} = 0 \tag{1.2}$$

where p is the kinematic pressure, $\nabla = \left(\partial/\partial x, \partial/\partial y\right)^T$ is the Nabla-operator, $\mathbf{D}$ is the small-scale dissipation supplied by the eddy viscosity model (EVM) and $\mathbf{F}$ is the external stochastic forcing. Let us introduce vorticity $\omega = \partial u_y/\partial x - \partial u_x/\partial y$ and stream function ψ satisfying the relation $\omega = \Delta\psi$, where $\Delta = \nabla \cdot \nabla$ is the Laplacian operator. Then velocity is given by $\mathbf{u} = \left(-\partial\psi/\partial y, \partial\psi/\partial x\right)^T$.

As an initial condition, we take unstable jet solution proposed in [16] with slight modifications:

$$u_x|_{t=0} = \exp\left(\frac{\pi^2}{2\sigma^2}\right) \cdot \exp\left[\frac{\pi^4}{2\sigma^2} \cdot \frac{1}{y(y-2\pi)}\right] \tag{1.3}$$

$$u_y|_{t=0} = 0. \tag{1.4}$$

For the convenience, also the spatial average is subtracted (not shown in formula). The velocity field (1.3) is infinitely differentiable in Ω and defined to be zero at the boundaries $y = 0, y = 2\pi$. Velocity takes its maximum value equal 1 at the center of the channel ($y = \pi$). Let us notice that velocity profile (1.3) is quasi-Gaussian since expanding expression in square brackets in Taylor series at the $y = \pi$, we obtain the Gaussian with variance σ^2:

$$\exp\left[\frac{\pi^4}{2\sigma^2} \cdot \frac{1}{y(y-2\pi)}\right] = \exp\left[-\frac{\pi^2}{2\sigma^2} - \frac{1}{2\sigma^2}(y-\pi)^2 + O((y-\pi)^4)\right].$$

1.1 Numerical methods

Numerical methods used are implemented in the package [27]. Spatial computational grid is uniform and staggered with mesh step h. Arrangement of variables corresponds to Arakawa 'C' grid, i.e., pressure is placed in the center of the computational cell, i.e., its coordinates with respect to the left-bottom cell corner are $(h/2, h/2)$, vorticity and stream function are located in the corner $(0, 0)$ while velocities are specified in the middles of the edges, u in $(0, h/2)$ and v in $(h/2, 0)$. Time step Δt satisfies Courant–Friedrichs–Lewy condition (CFL $= U_{\max}\Delta t/h < 0.2$). Equations (1.1), (1.2) are solved using projection method [8] with temporal approximation according to Adamsh–Baschforth rule (for any φ):

$$\varphi^{n+1/2} = \frac{3}{2}\varphi^n - \frac{1}{2}\varphi^{n-1} \tag{1.5}$$

where n is the number of time layer. We apply central difference scheme to the advection term which is energy-conserving provided the proper numerical analogue for the continuity equation is chosen [26] (here and below, summation is assumed for the repeating indices $i, j = 1, 2$):

$$\frac{\partial(u_i u_j)}{\partial x_j} \approx \delta_{x_j}(\overline{u_i}^{x_j}\overline{u_j}^{x_i}) \tag{1.6}$$

where the following operators are used:

$$\delta_{x_i}\varphi = \frac{\varphi(x_i + h/2) - \varphi(x_i - h/2)}{h}, \qquad \overline{\varphi}^{x_i} = \frac{\varphi(x_i + h/2) + \varphi(x_i - h/2)}{2}. \tag{1.7}$$

1.2 Eddy viscosity model (EVM) and external forcing

We use EVM model [19] based on the biharmonic operator,

$$D_i = -2 \cdot \frac{\partial}{\partial x_j}(\nu \Delta S_{ij}) \tag{1.8}$$

with Smagorinsky-like viscosity coefficient $\nu = C_{\text{smag}} h^4 |S|$, $C_{\text{smag}} = 0.06$ (see [22]), $S_{ij} = \frac{1}{2}(\partial u_i/\partial x_j + \partial u_j/\partial x_i)$ is the strain tensor and $|S| = \sqrt{2S_{ij}S_{ij}}$ is its modulus.

The external forcing $\mathbf{F}$ simulates an influence of the atmosphere on the ocean in the mesoscale atmospheric range where energy spectrum slope is $-5/3$ (see [29]). Each time step, we generate stream function of 'atmospheric flow' $\psi^F(x, y)$ in Fourier space with the following energy ($E = \frac{1}{2}\int |\nabla\psi|^2 \mathrm{d}\Omega = \int E(k)\mathrm{d}k$) distribution over wavenumbers: $E(k) = k^{-5/3}\exp[-(k/k^F)^8]$, where k^F is the wavenumber of cutting off introduced to ensure the fast convergence of statistical features with the increase of resolution. Fourier coefficients of ψ^F are

chosen to be uncorrelated discrete-time white noises under the assumption that atmospheric time scales are small enough. Given ψ^F, we compute the 'atmospheric' velocity field $(u_x^F, u_y^F) = (-\partial\psi^F/\partial y, \partial\psi^F/\partial x)$ and then preliminary forcing, $f_i = u_i^F|\mathbf{u}^F|$, via bulk formula for turbulent drag. Spatial average and divergent part of $\mathbf{f}$ are subtracted. Introducing amplitude A, we can control forcing power. Numerical integration of the forcing with forward Euler method gives a simple expression for the energy input [1]:

$$F_i = Af_i \tag{1.9}$$

$$\left\langle \frac{\partial|\mathbf{u}|^2/2}{\partial t} \right\rangle = \cdots + \frac{\Delta t}{2}\langle F_1^2 + F_2^2\rangle = \cdots + \frac{A^2\Delta t}{2}\langle f_1^2 + f_2^2\rangle \tag{1.10}$$

where brackets $\langle\cdot\rangle$ stand for ensemble averaging. In program we simply use spatial averaging as unbiased estimator of ensemble averaging since f_i are identically distributed in each mesh node.

1.3 Simulation parameters

Equations (1.1), (1.2) are integrated until $t = 25$ for the ensemble consisting of 100 realizations of the stochastic external forcing. We adjust the forcing amplitude A to provide energy input at a rate of 1% of initial energy during the full integration time. The reference model has resolution 512×512. Model with intermediate resolution (128×128) is used to show the convergence of statistics. Turbulence closures are analyzed for coarse-resolution models (32×32, 64×64). The external forcing ($\mathbf{F}$) and initial conditions (1.3) are well resolved on the computational grids: cutting off wavenumber for $\mathbf{F}$ is $k^F = 8$ which is twice less than maximum resolved wavenumber for the coarsest grid 32×32 ($k_{\max} = 16$). A width of the initial jet is $2\sigma = 1/2$. Bearing in mind Fourier transform of Gaussian distribution, $|\mathbb{F}(u_x|_{t=0})|^2 \sim \exp[-k_y^2\sigma^2]$, cutting off wavenumber for the initial jet is $k_y = 4$ which is again less than $k_{\max}$.

2 Statistical properties of barotropic instability

The stochastic forcing $\mathbf{F}$ allows for the introducing of ensemble averaging over its realizations denoted by angle brackets, $\langle\cdot\rangle$. Using ensemble averaging, we decompose the velocity field, $\mathbf{u}$, into the mean flow, $\langle\mathbf{u}\rangle$, and the turbulent fluctuations, $\mathbf{u}'$, what is also known as Reynolds decomposition:

$$\mathbf{u} = \langle\mathbf{u}\rangle + \mathbf{u}'. \tag{2.1}$$

Our main goal is to introduce statistical characteristics of turbulent fluctuations suitable to analyze solutions to the equations (1.1), (1.2). For this reason, we will consider approximate linear equations for $\mathbf{u}'$ derived under the assumptions that turbulent fluctuations are small (i.e., nonlinear terms $(\mathbf{u}'\cdot\nabla)\mathbf{u}'$ are negligible) and viscosity is negligible (inviscid limit). These two assumptions ensure that the mean flow is stationary, i.e., $\langle\mathbf{u}(t)\rangle = \mathbf{u}(0)$, where $\mathbf{u}(0)$ is given by (1.3), (1.4). Bearing in mind that Eddy viscosity model (1.8) depends on the mesh step, we conclude that inviscid limit corresponds to the infinitely high resolution.

To perform linearization, we write out 'barotropic vorticity equation' equivalent to (1.1), (1.2), see [35], and neglect viscosity:

$$\frac{\partial\Delta\psi}{\partial t} + J(\psi, \Delta\psi) = f_\omega \tag{2.2}$$

where $J(\psi, \Delta\psi) = -\partial\psi/\partial y \cdot \partial\Delta\psi/\partial x + \partial\psi/\partial x \cdot \partial\Delta\psi/\partial y$ is the Jacobian and $f_\omega = \partial F_y/\partial x - \partial F_x/\partial y$ is the stochastic forcing $\mathbf{F}$ in vorticity representation. Substituting decomposition $\psi = \psi_0 + \psi'$, where $\psi_0(y)$ is the initial flow (1.3), (1.4) in stream function representation, into (2.2) and neglecting nonlinear terms, we come to the linear equation for the turbulent fluctuations:

$$\frac{\partial\psi'}{\partial t} = A(y)\psi' + f_\psi \tag{2.3}$$

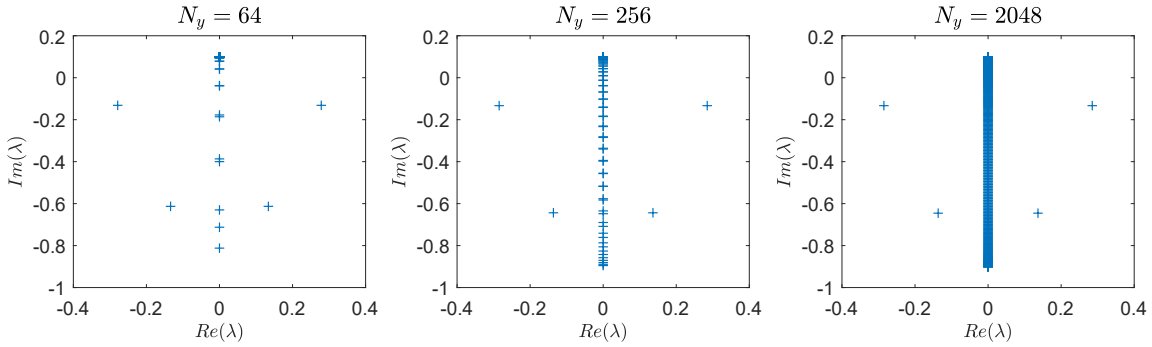

Fig. 1: Eigenvalues of matrix H for $k_x = 1$ and different N_y.

where

$$A(y) = \Big[\Delta^{-1}\Big(\frac{\mathrm{d}\psi_0(y)}{\mathrm{d}y}\Delta - \frac{\mathrm{d}^3\psi_0(y)}{\mathrm{d}y^3}\Big)\frac{\partial}{\partial x}\Big]\psi'$$

and $f_\psi = \Delta^{-1} f_\omega$ is the stochastic forcing in stream function representation. Here we assume that all functions belong to linear subspace of functions with zero integral value, i.e., for any $\varphi(x, y)$ we have $\int \varphi(x, y)\mathrm{d}x\mathrm{d}y = 0$, where Laplace operator Δ is invertible. Solution to equation (2.3) is dominated by the most fast-growing normal modes excited by the stochastic external forcing. As the main statistical property of barotropic instability arising in equations (1.1), (1.2), we have chosen some norm of the normal modes found in turbulent fluctuations.

2.1 Numerical solution of an eigenvalue problem

We start with eigenvalue problem $A(y)\Psi(x, y) = \lambda\Psi(x, y)$ which can be simplified taking into consideration that $A(y)$ is independent of x. Separating variables, $\Psi(x, y) \equiv \Psi(y)\mathrm{e}^{\mathrm{i}k_x x}$, where i is the imaginary unit, $k_x \in \mathbb{Z} \setminus 0$ ($k_x = 0$ corresponds to trivial stationary modes), we come to the 1D eigenvalue problem for $\Psi(y)$:

$$\Big(\frac{\mathrm{d}^2}{\mathrm{d}y^2} - k_x^2\Big)^{-1}\Big(\frac{\mathrm{d}\psi_0(y)}{\mathrm{d}y}\Big(\frac{\mathrm{d}^2}{\mathrm{d}y^2} - k_x^2\Big) - \frac{\mathrm{d}^3\psi_0(y)}{\mathrm{d}y^3}\Big)\mathrm{i}k_x\Psi(y) = \lambda\Psi(y). \tag{2.4}$$

Eigenvalue problem (2.4) has been solved numerically. Let us introduce uniform mesh along y direction with N_y nodes and step $h_y = 2\pi/N_y$. Coordinates of nodes are:

$$y_j = jh_y, \quad j = 0, \ldots, N_y - 1. \tag{2.5}$$

Approximation of $\mathrm{d}^2/\mathrm{d}y^2$ using second-order finite differences is denoted as matrix L, unit matrix as E. Matrices M_1 and M_2 are defined as follows: $M_1 = \mathrm{diag}(\mathrm{d}\psi_0(y)/\mathrm{d}y\big|_{y_i})$ and $M_2 = \mathrm{diag}(\mathrm{d}^3\psi_0(y)/\mathrm{d}y^3\big|_{y_i})$. Then finite-difference analogue of (2.4) is

$$H(k_x)\Psi = \lambda\Psi, \quad \Psi \in \mathbb{C}^{N_y}, \quad H(k_x) \in \mathbb{C}^{N_y \times N_y} \tag{2.6}$$

where matrix H depends on the k_x as follows: $H(k_x) = (L - k_x^2 E)^{-1}(M_1(L - k_x^2 E) - M_2)\mathrm{i}k_x$. For $k_x \in \mathbb{N}$ we solve full eigenvalue problem (2.6). Convergence of leading eigenvalues, i.e., $\max(\mathrm{Re}(\lambda))$, with respect to the number of mesh nodes N_y is shown in Fig. 1 for $k_x = 1$. For other k_x pictures are similar. Eigenvalues with $\mathrm{Re}(\lambda) > 0$ are separated from the rest spectrum and thus they are simple eigenvalues. Due to the special structure of the matrix H ($\mathrm{Re}(H) = 0$), these eigenvalues occur in pairs, $H\Psi = \lambda\Psi$ and $H\overline{\Psi} = -\overline{\lambda}\,\overline{\Psi}$ (overline stands for the complex conjugate), and it is seen in Fig. 1. For negative wavenumbers k_x, eigenvectors are the same and eigenvalues are simply $-\lambda$ since $H(-k_x) = -H(k_x)$. Finally, real-valued normal modes are composed of two eigenvectors ($H(k_x)\Psi = \lambda\Psi$ and $H(-k_x)\overline{\Psi} = \overline{\lambda}\,\overline{\Psi}$) and have the following form:

$$\Psi(y)\mathrm{e}^{\mathrm{i}k_x x}\mathrm{e}^{\lambda t} + \overline{\Psi(y)}\mathrm{e}^{-\mathrm{i}k_x x}\mathrm{e}^{\overline{\lambda}t} \equiv 2\mathrm{Re}(\Psi(y)\mathrm{e}^{\mathrm{i}k_x x}\mathrm{e}^{\lambda t}). \tag{2.7}$$

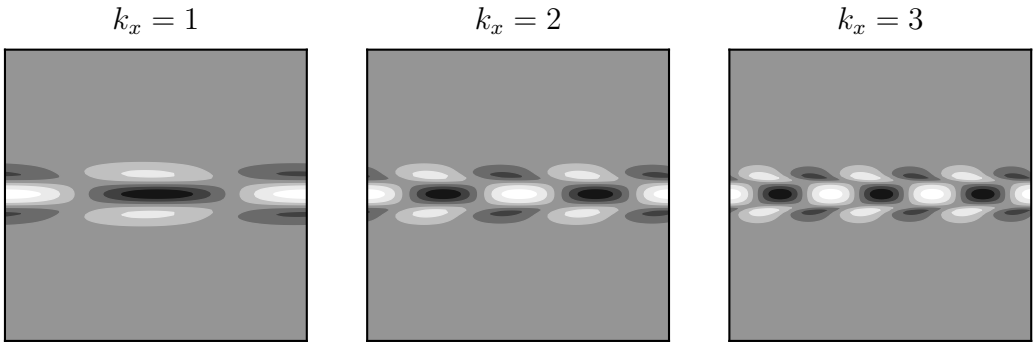

Fig. 2: The most excited in the numerical experiments normal modes of $A(y)$ in vorticity representation (real-valued part). The minimum value is in black, the maximum value is in white.

Tab. 1: Growth rates of normal modes for different k_x.

k_x	1	2	3	4	5
2Re(λ)	**0.5704** 0.2732	**0.9861** 0.3414	**1.0539** 0.0864	0.7949	0.2682

Normal modes are calculated in mesh with $N_y = 2048$. Among all $k_x \in \mathbb{N}$, spectrum of $A(y)$ has 8 growing ($\mathrm{Re}(\lambda) > 0$) normal modes. Growth rates of energy ($2\mathrm{Re}(\lambda)$) are given in Table 1. The most excited in the numerical experiments normal modes are in bold and shown in Fig. 2. They consume large energy from the external forcing or have huge enough growth rate, as will be shown in Section 2.3. Below we will work with these three normal modes, identifying them by the wavenumbers ($k_x = 1, 2, 3$) or by the ordinals (1st, 2nd, 3rd mode).

2.2 Projection onto a normal mode

Our goal is to project turbulent fluctuations $\mathbf{u}'$ (see (2.1)) found in numerical solutions of the nonlinear equations (1.1), (1.2) onto the subspace spanned by the desired normal mode of (2.3) to track its excitation. The projector we constructed is spectral in the sense that it projects parallel to invariant subspace of the matrix $H(k_x)$.

Now let us get real-valued $\psi'(x, y)$ in numerical experiment. Firstly, we perform Fourier expansion in x-variable:

$$\psi'(x, y) = \sum_{k_x \in \mathbb{Z}} \psi'_{k_x}(y) \mathrm{e}^{\mathrm{i}k_x x}. \tag{2.8}$$

Relation excluding complex-valued solutions is the following: $\psi'_{-k_x}(y) = \overline{\psi'_{k_x}(y)}$. That is why we restrict ourselves to the case $k_x > 0$. Subspaces corresponding to different k_x are invariant and moreover orthogonal with respect to $L_2(\Omega)$ inner product. We exclude x-dependence performing orthogonal projection which is spectral itself:

$$\psi'_{k_x}(y)\mathrm{e}^{\mathrm{i}k_x x} = \mathrm{e}^{\mathrm{i}k_x x} \frac{1}{2\pi} \int \psi'(x, y)\mathrm{e}^{-\mathrm{i}k_x x} \mathrm{d}x. \tag{2.9}$$

Now let ψ'_{k_x} be a vector representing function $\psi'_{k_x}(y)$ on a uniform vertical grid (2.5). For leading eigenvalue λ corresponding to given k_x we find two eigenvectors: $H(k_x)\Psi = \lambda\Psi$ and $H^*(k_x)\tilde{\Psi} = \overline{\lambda}\tilde{\Psi}$ (or equivalently left eigenvector), where '*' stands for the conjugate matrix transpose. Left eigenvector is known to perform spectral projection:

$$\frac{\tilde{\Psi}^* \psi'_{k_x}}{\tilde{\Psi}^* \Psi} \Psi. \tag{2.10}$$

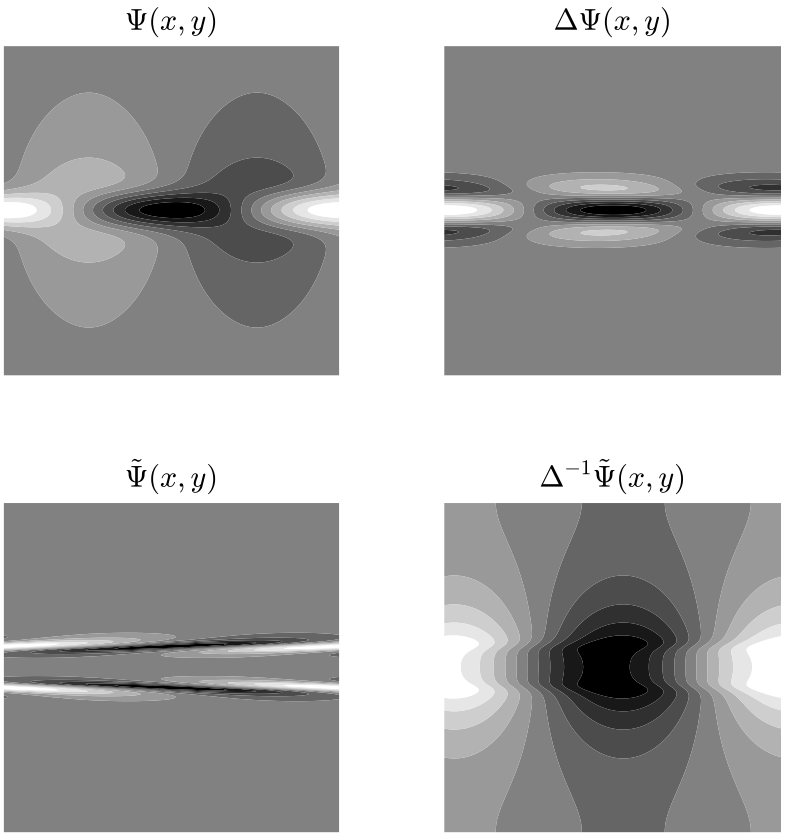

Fig. 3: Left column: normal mode $\Psi(x, y)$ and its projector $\tilde{\Psi}(x, y)$. Right column: the same, but in vorticity representation. Real-valued parts. Corresponds to leading eigenvalue for $k_x = 1$. The minimum value is in black, the maximum value is in white.

Finally, to show the resulting projection operator, we change inner product on mesh (2.5) with $L_2(0, 2\pi)$ inner product (it is reasonable since the former multiplied by mesh step h_y is the approximation of the latter), associate functions $\Psi(x, y) \equiv \Psi(y)e^{ik_x x}$, $\tilde{\Psi}(x, y) \equiv \tilde{\Psi}(y)e^{ik_x x}$ with vectors Ψ, $\tilde{\Psi}$ and apply consequently (2.9) and (2.10):

$$\psi'(x, y) \to 2\mathrm{Re}\left(\frac{\int \overline{\tilde{\Psi}(x, y)}\psi'(x, y)\mathrm{d}\Omega}{\int \overline{\tilde{\Psi}(x, y)}\Psi(x, y)\mathrm{d}\Omega}\Psi(x, y)\right). \tag{2.11}$$

Normal modes of (2.3) are of interest to us. So, we use maximum available resolution $N_y = 2048$ to find $\Psi(x, y)$ and $\tilde{\Psi}(x, y)$ and then interpolate them to the grid of the nonlinear model (1.1), (1.2). After that, all integrals in (2.11) are found numerically using simple rectangle rule. Functions $\Psi(x, y)$ and $\tilde{\Psi}(x, y)$ are shown in Fig. 3, $\tilde{\Psi}(x, y)$ has very tiny spatial structure debatable for 32^2 grid. So, it was decided to perform projection in vorticity representation where projector $\Delta^{-1}\tilde{\Psi}(x, y)$ and normal mode $\Delta\Psi(x, y)$ are smooth together, see right column in Fig. 3.

2.3 Growth-law for a normal mode

Projecting equation (2.3) onto the subspace spanned by the normal mode, we come to the following equation for the coefficient of normal mode α:

$$\mathrm{d}\alpha = \lambda\alpha\mathrm{d}t + \sigma\mathrm{d}W, \quad \alpha(0) = 0 \tag{2.12}$$

where σdW is the projection of the stochastic forcing f_ψ onto the normal mode, $\sigma > 0$, W is the complex Wiener process, i.e., $\langle\overline{\mathrm{d}W}\mathrm{d}W\rangle = \mathrm{d}t$. Solving (2.12) for growing normal modes ($\mathrm{Re}(\lambda) > 0$), we obtain the

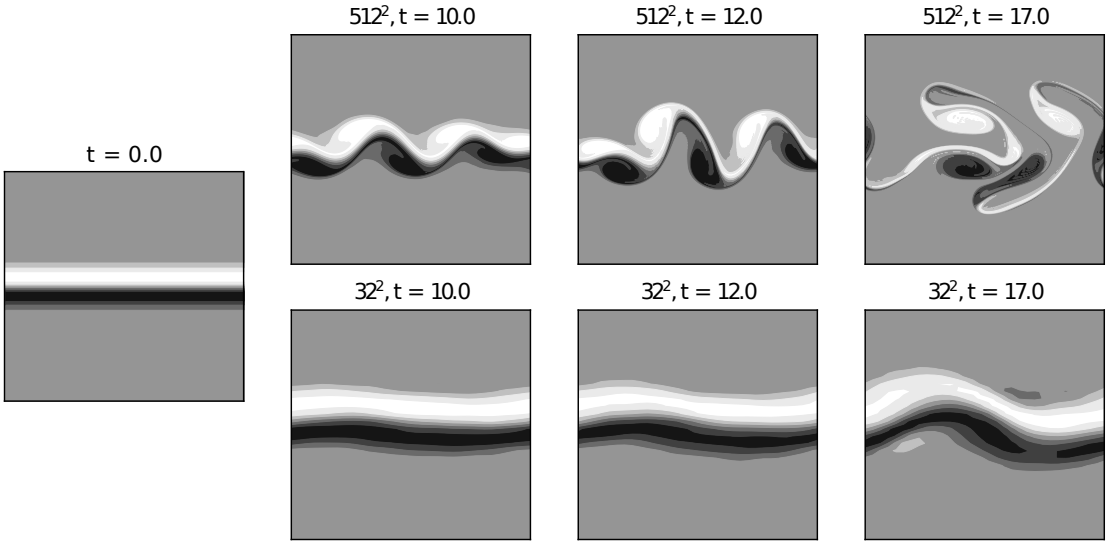

Fig. 4: Vorticity in different instants of time. Reference model (512^2) is in upper panel, coarse model (32^2) is in lower panel. The minimum value is in black, the maximum value is in white.

following expression for α (see [2]):

$$\langle |\alpha(t)|^2 \rangle = \frac{\sigma^2}{2\mathrm{Re}(\lambda)} (\mathrm{e}^{2\mathrm{Re}(\lambda)t} - 1). \tag{2.13}$$

Let us define ensemble-averaged energy of the normal mode $\Psi(x, y)$,

$$\langle E \rangle = \frac{\langle |\alpha|^2 \rangle}{2} \int |2\mathrm{Re}(\nabla \Psi)|^2 \mathrm{d}\Omega \tag{2.14}$$

and energy input into normal mode from the stochastic forcing, $\varepsilon = \frac{1}{2}\sigma^2 \int |2\mathrm{Re}(\nabla \Psi)|^2 \mathrm{d}\Omega$. Then for the ensemble-averaged energy of the normal mode, we have the following expression:

$$\langle E(t) \rangle = \frac{\varepsilon}{2\mathrm{Re}(\lambda)} (\mathrm{e}^{2\mathrm{Re}(\lambda)t} - 1). \tag{2.15}$$

For a long enough time ($t \gtrsim 1/\mathrm{Re}(\lambda)$), the energy $\langle E(t) \rangle$ of the normal modes grows with growth rate $2\mathrm{Re}(\lambda)$ while the pre-exponential factor is proportional to the forcing power ε.

2.4 Overview of simulations with different resolutions

In this section, we consider how do coarse-resolution models fail to reproduce barotropic instability and what are the main reasons for this.

We solve (1.1), (1.2) numerically for an ensemble of 100 realizations of the stochastic forcing using parameters given in Section 1.3. Solutions of reference (512^2) and coarse (32^2) models for two particular but different forcing realizations are shown in Fig. 4. The stochastic forcing excites normal modes which grow exponentially until $t \approx 10.0$ (in reference model) when turbulence starts. Instability grows slower in the coarse model (32^2) and its spatial pattern also different. Thus, bearing in mind that normal modes are different from each other in spatial pattern and growth rate, we conclude that at coarse resolution wrong normal modes grow, i.e., the most excited normal modes in coarse and reference solutions are different. Later we will show it precisely considering energy of normal modes separately. Let us notice that jet current is strongly smoothed out in the coarse model. It is caused by eddy viscosity since mean current $\langle \mathbf{u} \rangle$ (a function of y) is a stationary solution and unaffected by our advection scheme at any mesh resolution.

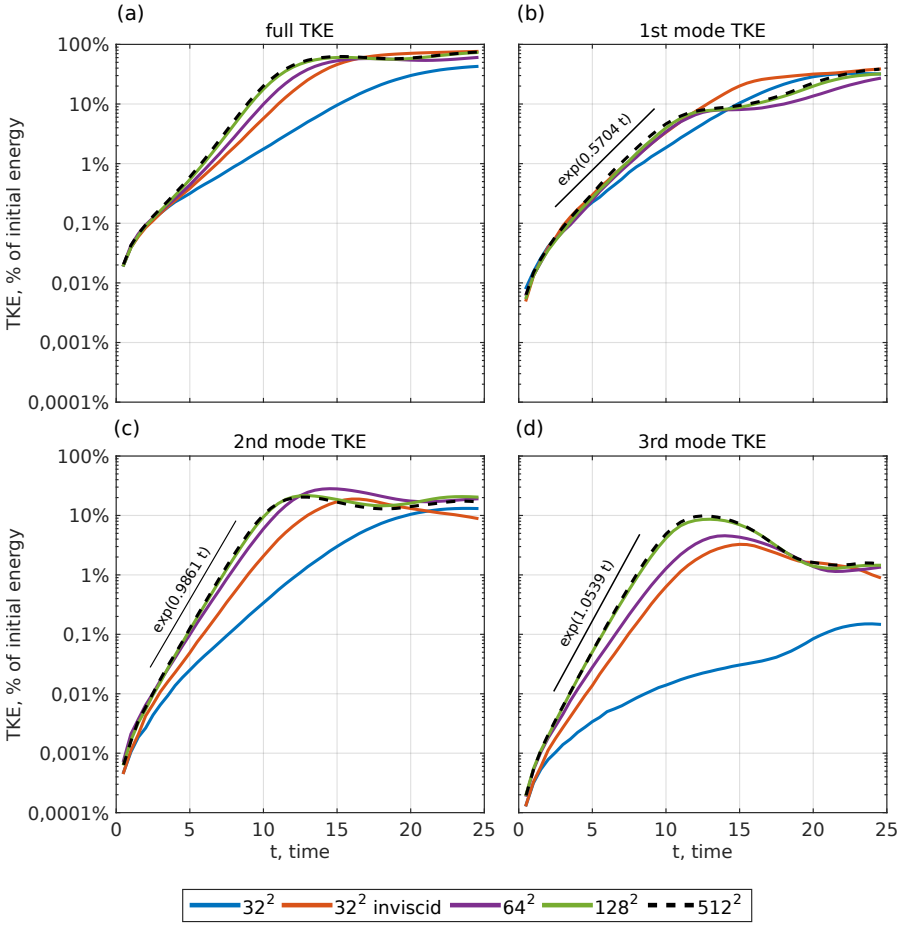

Fig. 5: Turbulence kinetic energy (TKE) (a) and TKE of normal modes $k_x = 1, 2, 3$, respectively (b), (c), (d), in % of initial jet energy. Blue, purple, green, and black lines are 32^2, 64^2, 128^2, 512^2 experiments, respectively. Red line corresponds to the inviscid simulation at 32^2 resolution.

We introduce the notion of turbulence kinetic energy (TKE):

$$\mathrm{TKE} = \frac{1}{2}\int \langle u_x'^2 \rangle + \langle u_y'^2 \rangle \mathrm{d}\Omega \tag{2.16}$$

where $\mathbf{u}'$ is the turbulent fluctuations, see (2.1). Angle brackets refer to averaging over an ensemble. By the notion 'normal mode TKE' we mean TKE of turbulent fluctuations projected onto normal mode using (2.11). In Fig. 5, for different resolutions, it is shown TKE (a) and TKE of normal modes (b-d) in % of initial jet energy. We notice convergence of these statistical characteristics with increasing of resolution.

First of all, let us describe results for the reference model (512^2). At the initial stage of instability, the TKE of normal modes grows linearly in logarithmic scale (see Figs. 5b–5d). Solid black lines show exponential growth with rates given in Table 1. As one can see, the slope of the TKE of normal modes in the reference model is close to the theoretical predictions given by linearized model. Vertical bias of the TKE of normal modes in logarithmic scale is determined by the pre-exponential factor, see (2.15), and depends on the value of the projection of the external forcing onto the normal mode which is decreasing with wavenumber (spectrum $k^{-5/3}$). Thus, initially dynamics is dominated by the 1st normal mode ($k_x = 1$), but later, fast-growing modes ($k_x = 2, 3$) become responsible for the transition to turbulence, which we define to occur at the bending point of TKE of normal modes ($t \approx 12$). Other normal modes mentioned in Table 1 have comparatively low energy level due to small projection of forcing and/or low growth rate.

Coarse-resolution models (32^2, 64^2) show underestimated TKE level compared to the TKE level of the reference model (512^2) (see Fig. 5a). It is explained by the reduced growth of small-scale normal modes. As

can be seen in Figs. 5b–5d, large-scale normal mode ($k_x = 1$) is reasonably well reproduced by coarse models while normal modes with smaller spatial scale ($k_x = 2, 3$) are damped. Damped 2nd and 3rd normal modes lead to wrong spatial structure and slowdown of instability as shown in Fig. 4.

Let us reveal the reasons for the fail of coarse models by considering two sources of errors: eddy viscosity model (EVM) which smoothes out the solution and numerical errors caused by finite resolution and numerical scheme. The influence of EVM was evaluated by performing additional inviscid integration of (1.1), (1.2) at coarse resolution 32^2 without EVM model, see line '32^2 inviscid' in Fig. 5. It follows from the figure that inviscid simulation is much closer to the reference model (512^2) compared to the viscid simulation (32^2), especially in the 3rd mode TKE level. Thus, the main reason for the slowdown of instability is the EVM model which can act in two ways: smoothing out the mean flow and reducing growth rates of normal modes of the linearized system. Additional experiments with the linearized model has shown smoothing of the mean flow to be crucial.

3 2D turbulence closures

In previous sections only EVM turbulence closure has been used. It must be applied in general circulation models (GCMs) to ensure numerical stability of the simulation when enstrophy transfer to unresolved scales occurs. As it was shown in previous section, turning off the EVM model can improve simulation of barotropic instability. Extending of this procedure to GCMs can be performed applying dynamic closure [17]. However, we are not familiar with works utilizing dynamic closure in GCMs. So, our strategy is to keep the EVM model without modifications and to try additional turbulence closures.

Together with enstrophy, EVM model also dissipates energy, which is prohibited by the KLB theory. To cure EVM models, 'energetically consistent' KEB parameterizations returning dissipated energy to the resolved scales have been developed [21, 22, 40]. Energy can be returned in a stochastic or deterministic way, and both of them have shown good results in restoring a mean flow [21] and spectrum of TKE [21, 33]. Below we will show that for the barotropic instability there is a substantial difference between the stochastic and deterministic KEB parameterizations.

3.1 Negative viscosity KEB (neg. visc.)

This parameterization was introduced in [21]. We add the following term to the right-hand side of (1.1):

$$\mu(t)\Delta\mathbf{u} \tag{3.1}$$

where $\mu(t) < 0$ is chosen at each time step to compensate energy dissipation of the EVM model:

$$\int \mathbf{D}\cdot\mathbf{u}\,\mathrm{d}\Omega + \mu(t)\int \Delta\mathbf{u}\cdot\mathbf{u}\,\mathrm{d}\Omega = 0 \tag{3.2}$$

where $\mathbf{D}$ was defined in (1.8).

3.2 Stochastic KEB (stoch)

Another one KEB parameterization is similar to one used in [20, 21]. At each time step, we construct two uncorrelated in space and with each other uniformly distributed on $(0, 1)$ random fields $\mathbf{s} = (s_1, s_2)$ defined in mesh nodes. Spatial mean and divergence are subtracted from these fields. Then we apply filter $G(\cdot) \equiv G_1(G_2(\cdot)) = G_2(G_1(\cdot))$ 6 times, where for any φ:

$$G_i(\varphi) = \frac{1}{6}\varphi(x_i - h) + \frac{2}{3}\varphi(x_i) + \frac{1}{6}\varphi(x_i + h). \tag{3.3}$$

According to [25], band width of 6 applications of filter (3.3) is $\Delta = \sqrt{6} \cdot 2h \approx 4.89h$. So, we inject energy into the scales slightly larger than dissipation scale of the EVM model which occurs the most extensively at $2h$ width. In [20] the fact that such filtration can also be viewed as a natural correction of the white-noise in space Reynolds tensor (used to describe influence of unresolved scales of motion) for the second-order numerical schemes is discussed.

After that, the fields (s_1, s_2) are substituted into the right-hand side of (1.1) and multiplied by the amplitude A (again, integrating using forward Euler method, the energy source is $\propto A^2$, see (1.10)) chosen to compensate the total energy dissipation by the EVM model:

$$\int \mathbf{D} \cdot \mathbf{u} \, \mathrm{d}\Omega + \frac{A^2 \Delta t}{2} \langle s_1^2 + s_2^2 \rangle = 0. \tag{3.4}$$

3.3 Scale-similarity model (SS)

Also we test nonlinear model not of the KEB type, namely SS model [4]:

$$f_i = -C \frac{\partial}{\partial x_j} \left(\widehat{u_i u_j} - \widehat{u_i} \widehat{u_j} \right) \tag{3.5}$$

where $\widehat{(\cdot)}$ is filter (3.3) and $C = 3$.

3.4 Difference between these parameterizations

Stochastic KEB does not affect the mean flow $\langle \mathbf{u} \rangle$ because of $\langle s_i \rangle = 0$. Also, it cannot modify the linearized system itself and thereby increase growth rates. Finally, the only impact from stochastic KEB is the exciting of normal modes while the majority of incoming energy is stored in non-growing normal modes which are not involved in the transition to turbulence. Negative viscosity KEB acts in another way. At the initial stage of instability growth, energy is returned mainly into the mean flow $\langle \mathbf{u} \rangle$ since $|\Delta \langle \mathbf{u} \rangle \cdot \langle \mathbf{u} \rangle| \gg |\Delta \mathbf{u}' \cdot \mathbf{u}'|$. Due to this fact, the energy of the mean flow is approximately conserved what prevents excess smoothing of mean flow and consequently increases the growth rates of normal modes.

SS model does not influence on jet current since (3.5) is zero for $u_i = U(y)\delta_{i,1}$, where $\delta_{i,j}$ is the Kronecker delta. On the other hand, it modifies the linearized system and, as will be shown in numerical experiments, the SS model increases the growth rates of normal modes.

4 Numerical experiments with KEB and SS parameterizations

We integrate equations (1.1), (1.2) again, adding into the right-hand side described above KEB and SS parameterizations. TKE characteristics for the model at resolution 32^2 are shown in Fig. 6. Negative viscosity and SS closures improve growth of the 2nd and 3rd normal modes in a similar way while SS closure improves the 1st normal mode slightly better. Bearing in mind that SS and negative viscosity closures act differently, namely the former affects the turbulent fluctuations and the latter affects the mean flow, we applied them together. Combined approach (neg.visc.+SS) substantially improves full TKE level and TKE of normal modes (see Fig. 6). Nevertheless, the 3rd normal mode still has too little energy. Hence, the 2nd normal mode has to grow longer, what slows down the transition to turbulence compared to the reference model. Solution snapshot for the combined model is shown in Fig. 7. Comparing with lower panel of Fig. 4, one can see that barotropic instability has acquired more correct spatial structure.

Results for the model at resolution 64^2 are shown in Fig. 8. Deterministic closures (neg. visc. SS and neg. visc.+SS) almost does not change TKE of the 1st and 2nd normal modes. The 3rd normal mode being too weak in bare model is greatly improved by the closures based on scale-similarity model (SS and neg. visc.+SS). Full

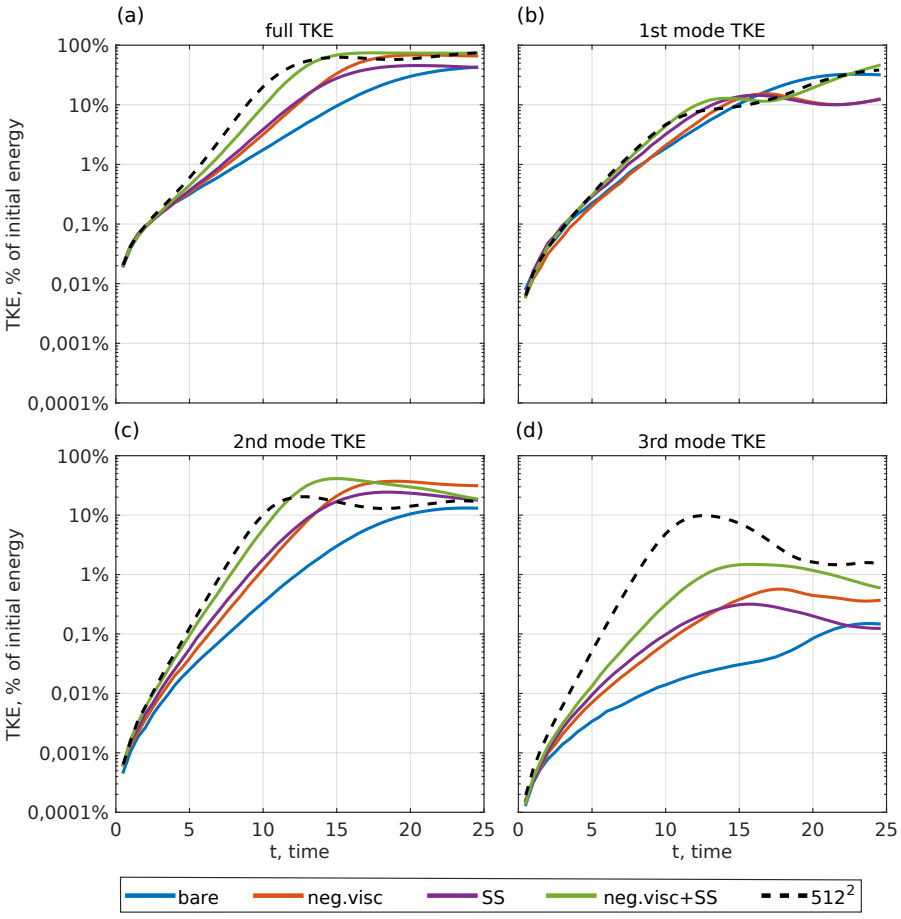

Fig. 6: Turbulence kinetic energy (TKE) (a) and TKE of normal modes $k_x = 1, 2, 3$, respectively (b), (c), (d), in % of initial jet energy. Results are shown for the model at resolution 32^2. Blue line ('bare') is the experiment without additional parameterizations. Red, purple, and green lines are the experiments with negative viscosity, scale-similarity, and combined (neg.visc+SS) parameterizations. Black line is the reference computation for the model at resolution 512^2.

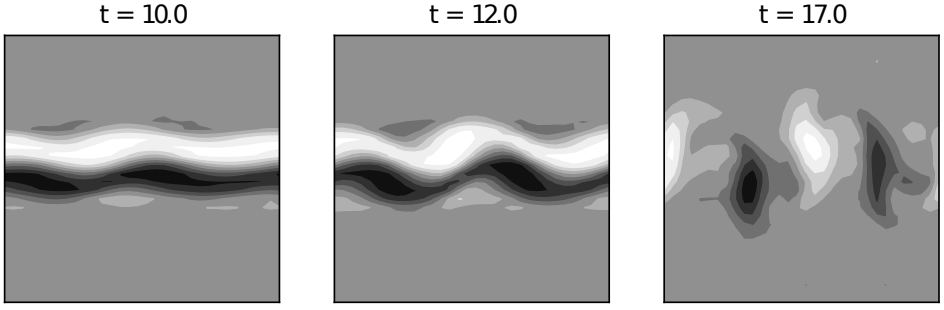

Fig. 7: Vorticity in different instants of time. Model at resolution 32^2 with combined (neg.visc.+SS) parameterization. The minimum value is in black, the maximum value is in white.

TKE is also approaching the reference level for these two closures. As one can see in Figs. 8b–8d, the stochastic KEB does not change the growth rates of normal modes but modify pre-exponential factors. Adjusting power of the stochastic KEB, the transition to turbulence can be accelerated. Majority of incoming energy is stored in non-growing normal modes that is why TKE level bias is large (see Fig. 8a). We do not show results for the stochastic KEB at resolution 32^2 because non-growing normal modes are strongly excited and TKE level is too different from the reference level.

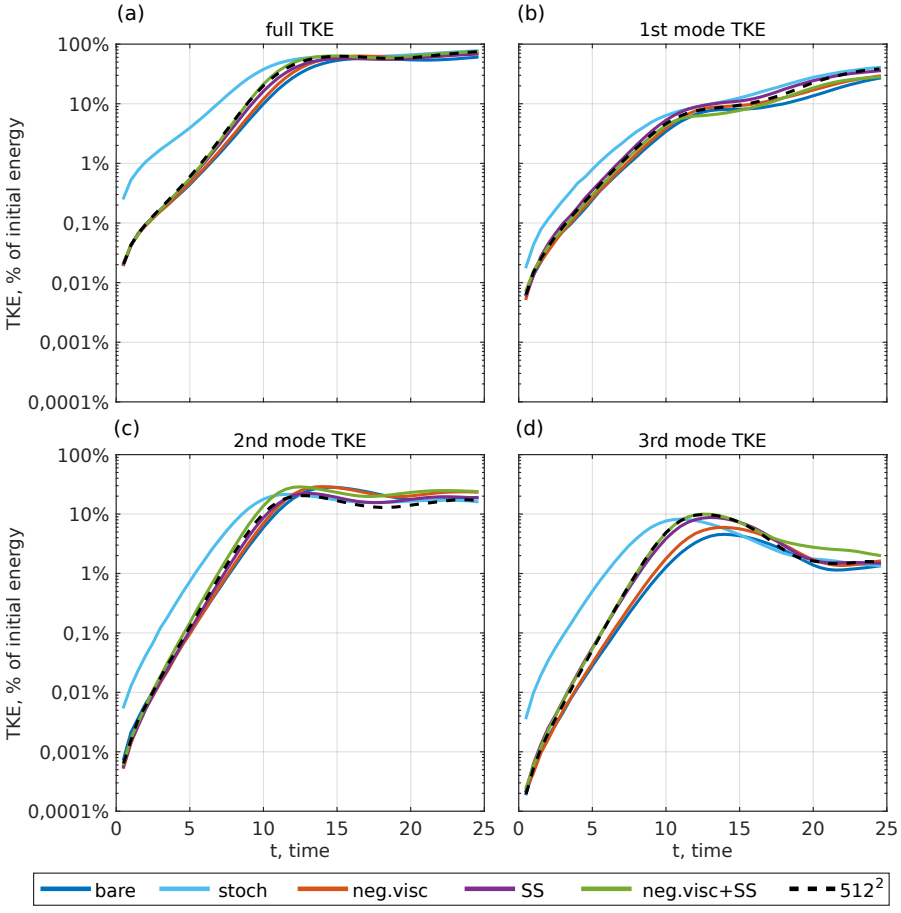

Fig. 8: The same as in Fig. 6, but for resolution 64^2. Additional light blue line is the experiment with stochastic KEB.

5 Conclusions

In the present work, the problem of numerical simulation of barotropic instability at coarse spatial resolutions is considered. Instability is excited by the external stochastic forcing allowing for the introducing of ensemble averaging. We focus on the initial stage of the barotropic instability when governing equations can be linearized to perform normal mode analysis. We assess the quality of coarse models, studying the growth of turbulence kinetic energy (TKE) and TKE of normal modes. We revealed the growth rates of normal modes to be substantially reduced at coarse resolutions of the model. It is due to numerical errors and eddy viscosity model. The latter smoothes out jet current, and it was shown to be the main reason for growth rates reduction.

Further, we studied the possibility of restoring the growth of normal modes without changing the eddy viscosity model. Three types of additional turbulence closures were considered: stochastic KEB, negative viscosity KEB, and scale-similarity model (SS). These parameterizations affect solution differently.

Negative viscosity KEB mainly influence on mean flow, preventing its smoothing and thereby increasing growth rates of normal modes. Scale-similarity model does not affect mean flow and modifies the linearized system, increasing growth rates of normal modes. Thus, we managed to find turbulence closure effectively changing the linear system itself. Given different principles of operation of these parameterizations, we combine them. The combined closure demonstrated the best results at coarse resolutions (32^2, 64^2).

In contrast to the developed turbulence case [21, 33], the barotropic instability simulation is strongly sensitive whether KEB closure is stochastic or deterministic. In developed turbulence, turbulent fluctuations prevail over mean flow, and any KEB returns energy into turbulent fluctuations where nonlinearity redistributes them analogously [33]. In the barotropic instability, stochastic KEB returns energy into turbulent fluctuations,

but negative viscosity KEB returns energy into the mean flow. Both deterministic and stochastic KEB accelerate the transition to turbulence. However, it happens not due to an increase of the growth rates of normal modes, but due to an increase of pre-exponentials. Wherein, the majority of incoming from stochastic KEB energy is stored in non-growing normal modes. If an aim is only to accelerate the transition to turbulence, then stochastic KEB can be used with reasonably moderate amplitude disposed in the regions of strong shear to prevent storing of energy in non-growing normal modes.

Summing up results of this work and [33], we are able to assess how do mentioned turbulence parameterizations work in complex situation when turbulence and jets appear in solution together. All three parameterizations are useful both in developed turbulence and in transition to turbulence and allow one to restore TKE spectrum and accelerate instability, respectively. Being tuned as in this work, they can be safely used in any higher resolved simulation because the limit of SS and KEB parameterizations (for fixed solution fields) as resolution approaches infinity equals zero.

Acknowledgment: Author would like to thank A. V. Glazunov, V. P. Dymnikov, and Yu. M. Nechepurenko for helpful comments and discussion.

Funding: This work was supported by the Russian Foundation for Basic Research (projects 19-35-90023, 18-05-60184).

References

[1] K. Alvelius, Random forcing of three-dimensional homogeneous turbulence. *Physics of Fluids* **11** (1999), No. 7, 1880–1889.
[2] L. Arnold, *Stochastic Differential Equations*. New York, 1974.
[3] N. Bakas and P. Ioannou, A theory for the emergence of coherent structures in beta-plane turbulence. *J. Fluid Mechanics* **740** (2014), 312–341.
[4] J. Bardina, J. Ferziger, and W. Reynolds, Improved subgrid-scale models for large-eddy simulation. In: *13th Fluid and Plasma Dynamics Conference*. 1980, p. 1357.
[5] G. Batchelor, Computation of the energy spectrum in homogeneous two-dimensional turbulence. *Physics of Fluids* **12** (1969), No. 12, II-233-II-239.
[6] J. Berner, G. Shutts, M. Leutbecher, and T. Palmer, A spectral stochastic kinetic energy backscatter scheme and its impact on flow-dependent predictability in the ECMWF ensemble prediction system. *J. Atmos. Sci.* **66** (2009), No. 3, 603–626.
[7] F. Bouchet, Parameterization of two-dimensional turbulence using an anisotropic maximum entropy production principle (2003). arXiv:cond-mat/0305205
[8] D. Brown, R. Cortez, and M. Minion, Accurate projection methods for the incompressible Navier–Stokes equations. *J. Comp. Phys.* **168** (2001), No. 2, 464–499.
[9] J. Chasnov, Simulation of the Kolmogorov inertial subrange using an improved subgrid model. *Physics of Fluids A: Fluid Dynamics* **3** (1991), No. 1, 188–200.
[10] J. Deardorff, A numerical study of three-dimensional turbulent channel flow at large Reynolds numbers. *J. Fluid Mechanics* **41** (1970), No. 2, 453–480.
[11] V. Dymnikov and P. Perezhogin, Systems of hydrodynamic type that approximate two-dimensional ideal fluid equations. *Izv. Atmos. Oceanic Phys.* **54**, No. 3, 232–241.
[12] G. Flato, J. Marotzke, B. Abiodun, P. Braconnot, S. Chou, W. Collins, P. Cox, F. Driouech, S. Emori, V. Eyring, and C. Forest, Evaluation of climate models. In: *Climate Change 2013: The Physical Science Basis. Contribution of Working Group I to the Fifth Assessment Report of the Intergovernmental Panel on Climate Change* **5** (2013), 741–866.
[13] J. Flor, *Fronts, Waves, and Vortices in Geophysical Flows*. Springer **805**, 2010.
[14] J. Frederiksen and A. Davies, Eddy viscosity and stochastic backscatter parameterizations on the sphere for atmospheric circulation models. *J. Atmos. Sci.* **54** (1997), No. 20, 2475–2492.
[15] J. Frederiksen and S. Kepert, Dynamical subgrid-scale parameterizations from direct numerical simulations. *J. Atmos. Sci.* **63** (2006), No. 11, 3006–3019.
[16] J. Galewsky, R. Scott, and L. Polvani, An initial-value problem for testing numerical models of the global shallow-water equations. *Tellus A: Dynamic Meteorology and Oceanography* **56** (2004), No. 5, 429–440.
[17] M. Germano, U. Piomelli, P. Moin, and W. Cabot, A dynamic subgrid-scale eddy viscosity model. *Physics of Fluids A: Fluid Dynamics* **3** (1991), No. 7, 1760–1765.

[18] A. Glazunov, Large-eddy simulation of turbulence with the use of a mixed dynamic localized closure: Part 1. Formulation of the problem, model description, and diagnostic numerical tests. *Izvestiya, Atmospheric and Oceanic Physics* **45** (2009), No. 1, 5–24.
[19] S. Griffies and R. Hallberg, Biharmonic friction with a Smagorinsky-like viscosity for use in large-scale eddy-permitting ocean models. *Monthly Weather Review* **128** (2000), No. 8, 2935–2946.
[20] I. Grooms, Y. Lee, and A. Majda, Numerical schemes for stochastic backscatter in the inverse cascade of quasigeostrophic turbulence. *Multiscale Modeling & Simulation* **13** (2015), No. 3, 1001–1021.
[21] M. Jansen and I. Held, Parameterizing subgrid-scale eddy effects using energetically consistent backscatter. *Ocean Modelling* **80** (2014), 36–48.
[22] M. Jansen, I. Held, A. Adcroft, and R. Hallberg, Energy budget-based backscatter in an eddy permitting primitive equation model. *Ocean Modelling*, **94** (2015), 15–26.
[23] R. Kraichnan, Inertial ranges in two-dimensional turbulence. *Physics of Fluids* **10** (1967), No. 7, 1417–1423.
[24] C. Leith, Diffusion approximation for two-dimensional turbulence. *Physics of Fluids* **11** (1968), No. 3, 671–672.
[25] T. Lund, On the use of discrete filters for large eddy simulation. In: *Annual Research Briefs. Center for Turbulence Research, NASA Ames-Stanford University.* 1997, pp. 83–95.
[26] Y. Morinishi, T. Lund, O. Vasilyev, and P. Moin, Fully conservative higher order finite difference schemes for incompressible flow. *J. Comp. Phys.* **143** (1998), No. 1, 90–124.
[27] E. Mortikov, Application of the immersed boundary method for solving the system of Navier–Stokes equations in domains with complex geometry. *Vychislitel'nye Metody i Programmirovanie* **11** (2010), No. 1, 32–42 (In Russian).
[28] B. Nadiga, Orientation of eddy fluxes in geostrophic turbulence. *Philosophical Transactions of the Royal Society of London A: Mathematical, Physical and Engineering Sciences.* **366** (2008), No. 1875, 2489–2508.
[29] G. Nastrom and K. Gage, A climatology of atmospheric wavenumber spectra of wind and temperature observed by commercial aircraft. *J. Atmos. Sci.* **42** (1985), No. 9, 950–960.
[30] P. Perezhogin, A. Glazunov, E. Mortikov, and V. Dymnikov, Comparison of numerical advection schemes in two-dimensional turbulence simulation. *Russ. J. Numer. Anal. Math. Modelling.* **32** (2017), No. 1, 47–60.
[31] P. Perezhogin and V. Dymnikov, Equilibrium states of finite-dimensional approximations of a two-dimensional incompressible inviscid fluid. *Nonlinear Dynamics* **13** (2017), No. 1, 55–79 (In Russian).
[32] P. Perezhogin and V. Dymnikov, Modeling of quasi-equilibrium states of a two-dimensional ideal fluid. *Doklady Physics* **62** (2017), No. 5, 248–252.
[33] P. Perezhogin, A. Glazunov, and A. Gritsun, Stochastic and deterministic kinetic energy backscatter parameterizations for simulation of the two-dimensional turbulence. *Russ. J. Numer. Anal. Math. Modelling* **34** (2019), No. 4, 197–213.
[34] P. Rhines, Waves and turbulence on a beta-plane. *J. Fluid Mechanics* **69** (1975), No. 3, 417–443.
[35] R. Salmon, *Lectures on geophysical fluid dynamics*. Oxford University Press, Oxford, 1998.
[36] G. Shutts and T. Palmer, Convective forcing fluctuations in a cloud-resolving model: Relevance to the stochastic parameterization problem. *J. Climate* **20** (2007), No. 2, 187–202.
[37] G. Shutts, A stochastic convective backscatter scheme for use in ensemble prediction systems. *Q. J. R. Meteorol. Soc.* **141** (2015), No. 692, 2602–2616.
[38] J. Smagorinsky, General circulation experiments with the primitive equations: I. The basic equations. *Monthly Weather Review* **91** (1963), No. 3, 99–164.
[39] G. Vallis, *Atmospheric and Oceanic Fluid Dynamics*. Cambridge University Press, Cambridge, 2017.
[40] P. Zurita-Gotor, I. Held, and M. Jansen, Kinetic energy-conserving hyperdiffusion can improve low resolution atmospheric models. *J. Advances Modeling Earth Systems* **7** (2015), No. 3, 1117–1135.